

Plug-and-Play Tri-Branch Invertible Block for Image Rescaling

Jingwei Bao^{1,2}, Jinhua Hao^{2*†}, Pengcheng Xu^{2*†}, Ming Sun², Chao Zhou², Shuyuan Zhu^{1*}

¹ University of Electronic Science and Technology of China, Chengdu, China

² Kuaishou Technology, Beijing, China

jwbao@std.uestc.edu.cn, {haojinhua, xupengcheng, sunming03, zhouchao}@kuaishou.com, eezsy@uestc.edu.cn

Abstract

High-resolution (HR) images are commonly downsampled to low-resolution (LR) to reduce bandwidth, followed by upscaling to restore their original details. Recent advancements in image rescaling algorithms have employed invertible neural networks (INNs) to create a unified framework for downscaling and upscaling, ensuring a one-to-one mapping between LR and HR images. Traditional methods, utilizing dual-branch based vanilla invertible blocks, process high-frequency and low-frequency information separately, often relying on specific distributions to model high-frequency components. However, processing the low-frequency component directly in the RGB domain introduces channel redundancy, limiting the efficiency of image reconstruction. To address these challenges, we propose a plug-and-play tri-branch invertible block (T-InvBlocks) that decomposes the low-frequency branch into luminance (Y) and chrominance (CbCr) components, reducing redundancy and enhancing feature processing. Additionally, we adopt an all-zero mapping strategy for high-frequency components during upscaling, focusing essential rescaling information within the LR image. Our T-InvBlocks can be seamlessly integrated into existing rescaling models, improving performance in both general rescaling tasks and scenarios involving lossy compression. Extensive experiments confirm that our method advances the state of the art in HR image reconstruction.

Code — <https://github.com/Jingwei-Bao/T-InvBlocks>

1 Introduction

High-resolution (HR) images are extensively distributed across online networks. To optimize display and conserve bandwidth and storage, HR images are typically downsampled to low-resolution (LR) versions that preserve visual integrity. Consequently, upscaling is essential to restore LR images to their original size and detail. Super-resolution methods (Dong et al. 2015; Dai et al. 2019; Chen et al. 2024; Qu et al. 2025; Qin et al. 2025) enhance image resolution but typically assume a predetermined, non-learnable downscaling operator. Recent studies (Kim et al. 2018; Xiao et al. 2020; Guo et al. 2022) have aimed to jointly optimize both

*Corresponding author.

†Project leader.

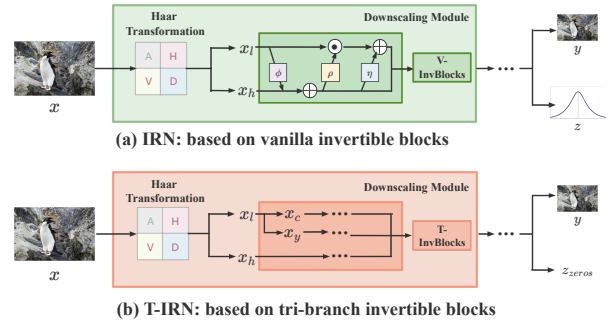


Figure 1: Comparison of IRN and T-IRN: (a) Vanilla invertible block in IRN processing low-frequency components in RGB. (b) Tri-branch invertible block in T-IRN processing low-frequency components in YCbCr, with separate branches for Y and CbCr.

downsampling and upscaling processes. IRN (Xiao et al. 2020) models the transformation between HR and LR images as a bijective mapping using an invertible neural network (INN) based on a vanilla invertible block (V-InvBlock) based on dual-branch. This method employs the Haar wavelet transform (Lienhart and Maydt 2002) to decompose the image into low- and high-frequency components, which are processed by an INN. The network enforces high-frequency components to follow a case-agnostic normal distribution, preserving as much information as possible, as shown in Figure 1(a). Additionally, LR images are often compressed to reduce bandwidth and storage (Son et al. 2021), but suffer quality degradation (Mo et al. 2025; Zhu et al. 2024). To address this, SAIN (Yang et al. 2023) builds on IRN by introducing an asymmetric model structure and incorporating simulated compression to enhance robustness. SAIN employs a learnable Gaussian mixture model (GMM) to sample and fit the lost high-frequency information during upscaling, based on the observed high-frequency distribution during downscaling.

Despite the widespread use of dual-branch invertible neural networks for image rescaling, we believe there is room for optimization. The V-InvBlock superficially addresses the interaction between high- and low-frequency components,

without fully exploring the integration of information across different domains to establish a more effective bijective mapping between LR and HR. The low-frequency components, preserved as the LR output, are the only intermediate result retained throughout the process and are crucial for restoring image details during upscaling, warranting further processing. Moreover, IRN’s ablation studies (Xiao et al. 2023) reveal that using an all-zero tensor instead of sampling from a Gaussian distribution can yield comparable or even superior upscaling results.

To address these issues, we propose a tri-branch invertible block that further decomposes the low-frequency branch into separate luminance (Y) and chrominance (CbCr) components. This approach is inspired by the understanding that luminance and chrominance belong to different domains of image information, each with distinct characteristics. By converting the low-frequency information into YCbCr color space and processing these components separately, the model reduces inter-channel redundancy, enhancing its ability to interact with and process different domains of image information more effectively. This approach improves the network’s capacity to accurately capture and reconstruct critical image details, thereby strengthening the overall quality of the rescaling transformation between LR and HR. Additionally, during upscaling in training process, we replace the high-frequency sampling operation with an all-zero tensor, a strategy aimed at concentrating the reconstruction task on the inherent details of the LR image itself, rather than relying on randomly sampled high-frequency information, as shown in Figure 1(b). This approach leverages the essential content within the LR image, which our experiments suggest leads to more accurate and robust HR reconstruction. We integrated our proposed blocks with the strategy into both IRN and SAIN, resulting in T-IRN and T-SAIN, which effectively demonstrate the plug-and-play nature of the T-InvBlock. This straightforward replacement of existing components without altering the overall network architecture allowed us to enhance performance across both general image rescaling tasks and scenarios involving lossy compression, highlighting the effectiveness and robustness of our approach.

Our main contributions are as follows:

- We introduce T-InvBlock, which separates the low-frequency RGB information into luminance (Y) and chrominance (CbCr) components. This reduces inter-channel redundancy and allows specialized processing of Y and CbCr, enhancing the model’s effectiveness in mapping LR to HR.
- We introduce a training strategy that replaces high-frequency sampling with an all-zero tensor, concentrating the information within the LR image, thereby reducing the risk of inconsistencies introduced by distribution sampling and enhancing the accuracy of restoration.
- We seamlessly integrate our block into existing IRN and SAIN models for both general rescaling and scenarios involving lossy compression of LR images. Experiments confirm the plug-and-play T-InvBlock’s effectiveness, and robustness, with improvements in performance.

2 Related Work

Image Rescaling. Super-resolution (SR) (Dong et al. 2015; Lim et al. 2017; Zhang et al. 2018b) aims to reconstruct HR images from LR inputs, which are typically down-scaled using algorithm like Bicubic interpolation, leading to the loss of high-frequency details. In contrast, image rescaling (Kim et al. 2018; Li et al. 2018; Sun and Chen 2020) jointly optimizes both downscaling and upscaling processes to better preserve image quality. Notably, IRN (Xiao et al. 2020) employs invertible neural networks (INNs) to model rescaling as a bijective transformation, where the downscaling and upscaling are not independent operations but are instead mutually inverse processes within the same model. The high-frequency components of the HR image are embedded into a case-agnostic latent space during downscaling, ensuring that as much information as possible is retained and can be accurately recovered during upscaling. HCFlow (Liang et al. 2021) extends this by integrating SR and rescaling tasks into a single framework, using conditional distributions for high-frequency details. BAIRNet (Pan et al. 2022) and IARN (Pan et al. 2023) introduce novel techniques like subpixel splitting and preemptive channel splitting to handle unconventional scaling factors. AIDN (Xing et al. 2023) further generalizes this approach by allowing for arbitrary scaling factors. In practical applications, downscaling is often paired with image compression, which can significantly degrade the quality of HR image reconstruction due to the loss of critical details in the compression process. To address this, SAIN (Yang et al. 2023) proposes an asymmetric invertible framework that simulates compression during downscaling and employs actual image codecs (e.g., JPEG) during upscaling, enhancing the model’s robustness to lossy compression when reconstructing HR images.

Invertible Neural Networks. Invertible Neural Networks (INNs), widely used in image rescaling, are derived from flow-based generative models. These networks ensure bijective mappings between source and target domains, allowing for precise transformations. Through normalizing flows (Rezende and Mohamed 2015; Kobyzev, Prince, and Brubaker 2020; Liu et al. 2021; Quan et al. 2024), INNs convert high-dimensional data, like images, into simple latent distributions such as Gaussian, enabling efficient computation of the Jacobian determinant and optimization of posterior probabilities via maximum likelihood estimation (MLE).

In the context of image rescaling tasks, the IRN model (Xiao et al. 2020) leverages a dual-branch invertible block (V-InvBlock) to process the HR image $x \in \mathbb{R}^{N \times H \times W \times C}$, decomposing it into low-frequency components $x_l \in \mathbb{R}^{N \times H \times W \times C/4}$ and high-frequency components $x_h \in \mathbb{R}^{N \times H \times W \times 3C/4}$ using the Haar wavelet transform. The low-frequency branch of IRN is based on the additive coupling layer introduced by (Dinh, Krueger, and Bengio 2014), while the high-frequency branch utilizes a more expressive affine coupling layer as proposed by (Dinh, Sohl-Dickstein, and Bengio 2016). The transformations applied in IRN are

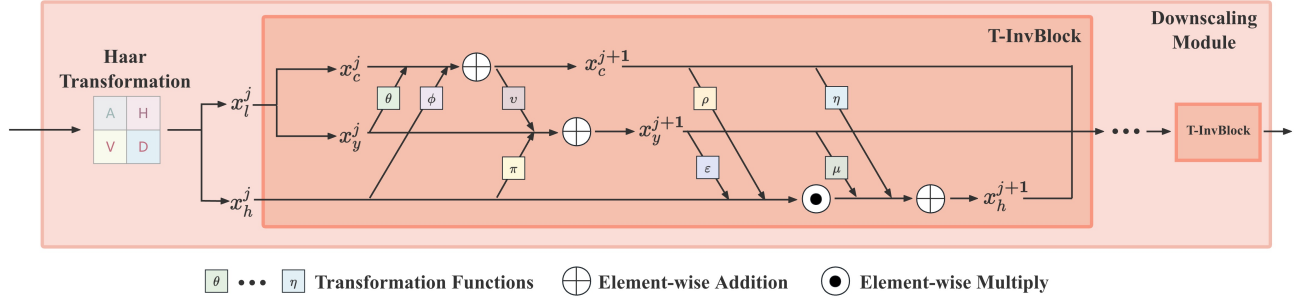


Figure 2: Architecture of tri-branch invertible block(T-InvBlock)

formalized as follows:

$$\begin{aligned}
 x_l^{j+1} &= x_l^j + \phi(x_h^j), \\
 x_h^{j+1} &= x_h^j \odot \exp(\rho(x_l^{j+1})) + \eta(x_l^{j+1}), \\
 x_h^j &= (x_h^{j+1} - \eta(x_l^{j+1})) \odot \exp(-\rho(x_l^{j+1})), \\
 x_l^j &= x_l^{j+1} - \phi(x_h^j).
 \end{aligned} \tag{1}$$

In the j -th block, x_l^j represents the low-frequency component, while x_h^j denotes the high-frequency component. These transformations ensure that the model effectively captures the essential details in both the low- and high-frequency domains, while maintaining the invertibility of the overall network. The transformation functions $\phi(\cdot)$, $\eta(\cdot)$, and $\rho(\cdot)$ are parameterized by densely connected convolutional blocks (Wang et al. 2018).

Additionally, SAIN (Yang et al. 2023) builds upon this V-InvBlock by introducing the Enhanced Invertible Block (E-InvBlock), which adds some transformation functions specifically for the downscaling module. However, the compression simulation module in SAIN retains the design of IRN, maintaining the V-InvBlocks with dual-branch structure, as shown in Figure 3(a).

3 Methodology

3.1 Preliminaries

In image rescaling tasks, dual-branch invertible neural networks, which process high and low-frequency components separately after Haar wavelet transformation, are widely adopted. IRN (Xiao et al. 2020) splits HR images x into low- and high-frequency components $[x_l, x_h]$, learning an invertible mapping $[x_l, x_h] \leftrightarrow [y, z]$, where y is the LR output and $z \sim \mathcal{N}(0, 1)$ is a case-agnostic variable. SAIN enhances robustness against image compression by establishing an asymmetric framework. Here, the downscaling process is modeled by f , which outputs a high-quality LR image y , and the compression is simulated by g . The combined operation $f \circ g$ then maps $[x_l, x_h]$ to $[\hat{y}, \hat{z}]$, where \hat{y} is the simulated compressed LR image. When compression artifacts, introduced by ϵ , degrade y to y' , the reverse pass first applies the inverse compression function g^{-1} to y' , recovering it to y_r . Then, the reverse pass reconstructs the HR image by mapping $[y_r, \hat{z}] \rightarrow x'$, with z modeled by a learnable GMM, as shown in Figure 3.

In this work, we propose our plug-and-play T-InvBlock for enhanced image rescaling. After applying the Haar wavelet transform, the low-frequency component x_l is converted to YCbCr color space and decomposed into x_y (luminance) and x_c (chrominance) channels, which are then processed through the T-InvBlock’s three branches. This structure reduces inter-channel redundancy and allows for more targeted processing of luminance and chrominance information. At the final stage of downscaling, x_y and x_c are concatenated, converted back to the original color space, and output as the LR image y . The model learns an invertible mapping $[x_y, x_c, x_h] \leftrightarrow [y, z]$, where during upscaling, z is set to an all-zero tensor. This approach shifts the responsibility of encoding high-frequency details from a statistical distribution (e.g., fixed Gaussian in IRN or learnable GMM in SAIN) to the LR image itself, concentrating relevant information within the LR representation. By seamlessly integrating the T-InvBlock into the IRN and SAIN frameworks, we developed T-IRN and T-SAIN, which, as illustrated in Figure 1(b) and Figure 3(b), demonstrated superior results across various rescaling tasks, including those involving lossy compression, thereby proving the effectiveness and versatility of our approach.

3.2 Tri-branch Invertible Block

Previous image rescaling methods using dual-branch invertible neural networks process low-frequency (x_l) and high-frequency (x_h) components from Haar wavelet transformation separately. We propose an improvement by converting x_l to YCbCr, decomposing it into luminance (Y) and chrominance (CbCr) components, and processing these through independent branches for more effective interaction and analysis. Given that x_l is the only element retained throughout the rescaling process, it warrants deeper processing.

Converting low-frequency information into the YCbCr color space and segregating the luminance (Y) from the chrominance (CbCr) components, rather than directly processing low-frequency RGB data, offers several significant advantages. This conversion effectively reduces inter-channel redundancy (Jain 1989; Poynton 2012), thereby enhancing the overall efficiency of information representation and allowing the model to concentrate more precisely on the critical features that influence image quality. Furthermore,

the distinct operational domains of luminance and chrominance facilitate the application of more tailored processing techniques for each component, which can lead to optimized performance outcomes. This strategy is especially advantageous in scenarios involving JPEG-compressed LR images, as JPEG compression inherently operates in the YCbCr domain (Wallace 1991). By aligning the model’s processing framework with this compression standard, the model is better equipped to adapt to compression artifacts, ultimately leading to superior reconstruction quality. As a result, we developed a novel downscaling module based on the T-InvBlock architecture, as illustrated in Figure 2.

Based on Equation 1, the T-InvBlock can be formulated as follows:

$$\begin{aligned}
 x_c^{j+1} &= x_c^j + \phi(x_h^j) + \theta(x_y^j), \\
 x_y^{j+1} &= x_y^j + \nu(x_c^{j+1}) + \pi(x_h^j), \\
 x_h^{j+1} &= x_h^j \odot \exp(\rho(x_c^{j+1}) + \varepsilon(x_y^{j+1})) \\
 &\quad + \eta(x_c^{j+1}) + \mu(x_y^{j+1}).
 \end{aligned}
 \tag{2}$$

The upscaling process is:

$$\begin{aligned}
 x_h^j &= (x_h^{j+1} - \eta(x_c^{j+1}) - \mu(x_y^{j+1})) \\
 &\quad \odot \exp(-\rho(x_c^{j+1}) - \varepsilon(x_y^{j+1})), \\
 x_y^j &= x_y^{j+1} - \nu(x_c^{j+1}) - \pi(x_h^j), \\
 x_c^j &= x_c^{j+1} - \phi(x_h^j) - \theta(x_y^j).
 \end{aligned}
 \tag{3}$$

In the j -th T-InvBlock, x_c^j represents the chrominance components, and x_y^j denotes the luminance component of the low-frequency information, while x_h^j represents the high-frequency component. The transformation functions $\phi(\cdot)$, $\theta(\cdot)$, $\nu(\cdot)$, $\pi(\cdot)$, $\rho(\cdot)$, $\varepsilon(\cdot)$, $\eta(\cdot)$, and $\mu(\cdot)$ are parameterized by densely connected convolutional blocks (Wang et al. 2018), similar to those used in the V-InvBlock, and are designed to handle the interactions and updates across the different components within the block.

3.3 All-zero mapping Strategy

We propose an all-zero mapping strategy for modeling high-frequency components during upscaling, aiming to enhance the performance of image rescaling tasks by more effectively utilizing the information within the LR image. This approach is inspired by two key observations. First, experiments with IRN show that using an all-zero tensor for the initial high-frequency component during upscaling can achieve similar or even better HR reconstruction performance than using tensors sampled from a fixed Gaussian distribution. This suggests that the precise modeling of high-frequency components may not be as crucial to final image quality as previously thought. Second, although the SAIN model employs a GMM to learn the latent distribution of high-frequency components, the official weights show that the GMM actually learns a near-zero mean unimodal distribution. This further indicates that high-frequency information in practice does not exhibit complex distribution characteristics, implying that a simple all-zero tensor may suffice for effective HR image reconstruction.

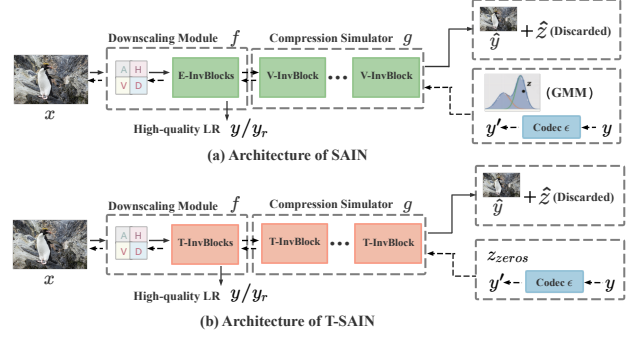


Figure 3: Architecture of SAIN and T-SAIN

Building on these insights, we adopt an all-zero tensor, i.e., $z = 0$, for high-frequency components during upscaling in models’ training and testing processes. This approach shifts the responsibility for representing high-frequency details to the LR image itself, which we hypothesize could offer a more deterministic and content-specific basis for reconstruction compared to abstract statistical models like fixed Gaussian distributions or learnable GMM, which introduce randomness that may not always align with the actual content of the image. Our experiments suggest that by mapping high-frequency information to an all-zero tensor, the model can more effectively utilize the inherent information within the LR image, leading to more accurate and robust HR reconstruction. This strategy leverages the essential content already present in the LR image, resulting in enhanced performance in the upscaling process.

3.4 T-IRN and T-SAIN

We enhanced the IRN and SAIN models by seamlessly integrating our newly designed T-InvBlock. This integration highlights the plug-and-play nature of the T-InvBlock, allowing us to replace the V-InvBlock or E-InvBlock in the original models without altering the overall network architecture. By introducing the T-InvBlock and implementing our all-zero mapping strategy, we developed the T-IRN and T-SAIN models. These enhanced models not only preserve the robustness and effectiveness of the original frameworks but also deliver significant performance improvements across various image rescaling tasks.

For T-IRN, the invertible blocks in the original downscaling module are substituted with T-InvBlocks. The all-zero mapping strategy eliminates the need for mapping high-frequency components to a distribution, making the original distribution matching loss $\mathcal{L}_{\text{distr}}$ unnecessary. Thus, the T-IRN training objective, inherited from IRN, omits this term and is expressed as follows:

$$\mathcal{L} = \lambda_1 \mathcal{L}_{hr} + \lambda_2 \mathcal{L}_{lr}.
 \tag{4}$$

Here, \mathcal{L}_{hr} ensures that the HR image x can be accurately restored from the model-downscaled LR image y using an all-zero tensor z , while \mathcal{L}_{lr} maintains the perceptual quality of the LR images by matching them to those produced by Bicubic interpolation. The terms λ_1 and λ_2 are the respective loss weights.

Downscaling & Upscaling	Scale	Param	Set5	Set14	BSD100	Urban100	DIV2K
Bicubic & Bicubic	2×	/	33.66 / 0.9299	30.24 / 0.8688	29.56 / 0.8431	26.88 / 0.8403	31.01 / 0.9393
Bicubic & SRCNN (Dong et al. 2015)	2×	57.3K	36.66 / 0.9542	32.45 / 0.9067	31.36 / 0.8879	29.50 / 0.8946	35.60 / 0.9663
Bicubic & EDSR (Lim et al. 2017)	2×	40.7M	38.20 / 0.9606	34.02 / 0.9204	32.37 / 0.9018	33.10 / 0.9363	35.12 / 0.9699
Bicubic & RDN (Zhang et al. 2018b)	2×	22.1M	38.24 / 0.9614	34.01 / 0.9212	32.34 / 0.9017	32.89 / 0.9353	–
Bicubic & RCAN (Zhang et al. 2018a)	2×	15.4M	38.27 / 0.9614	34.12 / 0.9216	32.41 / 0.9027	33.34 / 0.9384	–
Bicubic & SAN (Dai et al. 2019)	2×	15.7M	38.31 / 0.9620	34.07 / 0.9213	32.42 / 0.9028	33.10 / 0.9370	–
TAD & TAU (Kim et al. 2018)	2×	–	38.46 / –	35.52 / –	36.68 / –	35.03 / –	39.01 / –
CNN-CR & CNN-SR (Li et al. 2018)	2×	–	38.88 / –	35.40 / –	33.92 / –	33.68 / –	–
CAR & EDSR (Sun and Chen 2020)	2×	51.1M	38.94 / 0.9658	35.61 / 0.9404	33.83 / 0.9262	35.24 / 0.9572	38.26 / 0.9599
IRN(Xiao et al. 2020)	2×	1.67M	43.99 / 0.9871	40.79 / 0.9778	41.32 / 0.9876	39.92 / 0.9865	44.32 / 0.9908
T-IRN (Ours)	2×	1.57M	44.86 / 0.9883	41.70 / 0.9809	42.68 / 0.9913	41.05 / 0.9899	45.46 / 0.9932
Bicubic & Bicubic	4×	/	28.42 / 0.8104	26.00 / 0.7027	25.96 / 0.6675	23.14 / 0.6577	26.66 / 0.8521
Bicubic & SRCNN (Dong et al. 2015)	4×	57.3K	30.48 / 0.8628	27.50 / 0.7513	26.90 / 0.7101	24.52 / 0.7221	–
Bicubic & EDSR (Lim et al. 2017)	4×	43.1M	32.62 / 0.8984	28.94 / 0.7901	27.79 / 0.7437	26.86 / 0.8080	29.38 / 0.9032
Bicubic & RDN (Zhang et al. 2018b)	4×	22.3M	32.47 / 0.8990	28.81 / 0.7871	27.72 / 0.7419	26.61 / 0.8028	–
Bicubic & RCAN (Zhang et al. 2018a)	4×	15.6M	32.63 / 0.9002	28.87 / 0.7889	27.77 / 0.7436	26.82 / 0.8087	30.77 / 0.8460
Bicubic & ESRGAN (Wang et al. 2018)	4×	16.3M	32.74 / 0.9012	29.00 / 0.7915	27.84 / 0.7455	27.03 / 0.8152	30.92 / 0.8486
Bicubic & SAN (Dai et al. 2019)	4×	15.7M	32.64 / 0.9003	28.92 / 0.7888	27.78 / 0.7436	26.79 / 0.8068	–
TAD & TAU (Kim et al. 2018)	4×	–	31.81 / –	28.63 / –	28.51 / –	26.63 / –	31.16 / –
CAR & EDSR (Sun and Chen 2020)	4×	52.8M	33.88 / 0.9174	30.31 / 0.8382	29.15 / 0.8001	29.28 / 0.8711	32.82 / 0.8837
IRN(Xiao et al. 2020)	4×	4.35M	36.19 / 0.9451	32.67 / 0.9015	31.64 / 0.8826	31.41 / 0.9157	35.07 / 0.9318
T-IRN (Ours)	4×	4.67M	36.29 / 0.9452	32.70 / 0.9003	31.64 / 0.8837	31.19 / 0.9132	35.10 / 0.9328

Table 1: Quantitative evaluation results (PSNR / SSIM) of different downscaling and upscaling methods for image reconstruction on benchmark datasets: Set5, Set14, BSD100, Urban100, and DIV2K validation set.

For T-SAIN, we retained the asymmetric model framework and reconstructed the downscaling module f and compression simulator g using T-InvBlocks. Since SAIN does not use distribution-related guidance loss for the GMM during training, we adopted the same loss function as SAIN and replaced the GMM with the all-zero mapping strategy, as shown in Figure 3(b).

4 Experiments

4.1 Experimental Setup

Datasets and Settings. We adopt 800 HR images from the widely-used DIV2K training set (Agustsson and Timofte 2017) to train our models. For evaluation, T-IRN is assessed on five standard test sets: Set5 (Bevilacqua et al. 2012), Set14 (Zeyde, Elad, and Protter 2010), BSD100 (Martin et al. 2001), Urban100 (Huang, Singh, and Ahuja 2015), and the DIV2K validation set (Agustsson and Timofte 2017). T-SAIN is evaluated on the DIV2K validation set with JPEG compression at QFs (i.e., 30, 50, 70, 80, 90). While quality assessment methods are diverse (Yuan et al. 2024; Lu et al. 2024; Xie et al. 2024), following standard image rescaling practices (Xiao et al. 2020; Yang et al. 2023), both models are evaluated using Peak Signal-to-Noise Ratio (PSNR) and Structural Similarity Index (SSIM) (Wang et al. 2004), measured on the Y channel of the YCbCr color space.

Implementation Details. For T-IRN image rescaling, we use a single downscaling module (Haar transformation with 3 T-InvBlocks) for $\times 2$ scaling, and two modules with an additional T-InvBlock for $\times 4$. The $\times 2$ model is trained for 800k iterations, halving the learning rate every 100k iterations, while the $\times 4$ model is trained for 600k iterations, with

the learning rate halved every 40k iterations. Loss weights are set to $\lambda_1 = 1$ and $\lambda_2 = 0.25$ to balance LR and HR loss and enhance HR detail restoration.

For T-SAIN $\times 2$ image rescaling, we employ a single downscaling module and a T-InvBlock as a compression simulator, doubling the modules for $\times 4$. Both T-SAIN models are trained for 600k iterations, with the learning rate halved every 100k iterations. The training setup follows SAIN (Yang et al. 2023), including the loss function and JPEG codec ε with a QF of 75.

In all T-IRN and T-SAIN experiments, the initial learning rate is 2×10^{-4} , using \mathcal{L}_2 pixel loss for \mathcal{L}_{lr} and \mathcal{L}_1 pixel loss for \mathcal{L}_{hr} in RGB space. Input images are cropped to 128×128 and augmented with random flips. We use the Adam optimizer (Kingma and Ba 2014) with $\beta_1 = 0.9$, $\beta_2 = 0.999$, and a mini-batch size of 16.

4.2 Evaluation for T-IRN

Quantitative Evaluation. We compared T-IRN against two types of methods: (1) approaches based on Bicubic downscaling combined with super-resolution (Dong et al. 2015; Lim et al. 2017; Zhang et al. 2018b,a; Wang et al. 2018; Dai et al. 2019), and (2) methods that perform jointly-optimized downscaling and upscaling (Kim et al. 2018; Li et al. 2018; Sun and Chen 2020), especially original IRN (Xiao et al. 2020).

As shown in Table 1, T-IRN outperforms state-of-the-art baseline models, including IRN, in terms of PSNR and SSIM across all datasets. At the $\times 2$ scale, our method achieves a PSNR improvement of approximately 0.9 to 1.3 dB over IRN. Importantly, these improvements are not limited to the Y-channel; our method also shows a notable in-

Downscaling & Upscaling	Scale	Param	JPEG QF=30	JPEG QF=50	JPEG QF=70	JPEG QF=80	JPEG QF=90
Bicubic & Bicubic	×2	/	29.38 / 0.8081	30.19 / 0.8339	30.91 / 0.8560	31.38 / 0.8703	31.96 / 0.8878
Bicubic & SRCNN (Dong et al. 2015)	×2	57.3K	28.01 / 0.7872	28.69 / 0.8154	29.43 / 0.8419	30.01 / 0.8610	30.88 / 0.8878
Bicubic & EDSR (Lim et al. 2017)	×2	40.7M	28.92 / 0.7947	29.93 / 0.8257	31.01 / 0.8546	31.91 / 0.8753	33.44 / 0.9052
Bicubic & RDN (Zhang et al. 2018b)	×2	22.3M	28.95 / 0.7954	29.96 / 0.8265	31.02 / 0.8549	31.91 / 0.8752	33.41 / 0.9046
Bicubic & RCAN (Zhang et al. 2018a)	×2	15.4M	28.84 / 0.7932	29.84 / 0.8245	30.94 / 0.8538	31.87 / 0.8749	33.44 / 0.9052
CAR & EDSR (Sun and Chen 2020)	×2	51.1M	27.83 / 0.7602	28.66 / 0.7903	29.44 / 0.8165	30.07 / 0.8347	31.31 / 0.8648
IRN (Xiao et al. 2020)	×2	1.67M	29.24 / 0.8051	30.20 / 0.8342	31.14 / 0.8604	31.86 / 0.8783	32.91 / 0.9023
SAIN (Yang et al. 2023)	×2	2.02M	31.47 / 0.8747	33.17 / 0.9082	34.73 / 0.9296	35.46 / 0.9374	35.96 / 0.9419
T-SAIN (Ours)	×2	2.09M	31.89 / 0.8912	33.71 / 0.9210	35.20 / 0.9384	35.86 / 0.9443	36.30 / 0.9478
Bicubic & Bicubic	×4	/	26.27 / 0.6945	26.81 / 0.7140	27.28 / 0.7326	27.57 / 0.7456	27.90 / 0.7618
Bicubic & SRCNN (Dong et al. 2015)	×4	57.3K	25.49 / 0.6819	25.91 / 0.7012	26.30 / 0.7206	26.55 / 0.7344	26.84 / 0.7521
Bicubic & EDSR (Lim et al. 2017)	×4	43.1M	25.87 / 0.6793	26.57 / 0.7052	27.31 / 0.7329	27.92 / 0.7550	28.88 / 0.7889
Bicubic & RDN (Zhang et al. 2018b)	×4	22.3M	25.92 / 0.6819	26.61 / 0.7075	27.33 / 0.7343	27.92 / 0.7556	28.84 / 0.7884
Bicubic & RCAN (Zhang et al. 2018a)	×4	15.6M	25.77 / 0.6772	26.45 / 0.7031	27.21 / 0.7311	27.83 / 0.7537	28.82 / 0.7884
Bicubic & ESRGAN (Wang et al. 2018)	×4	16.3M	25.87 / 0.6803	26.58 / 0.7063	27.36 / 0.7343	27.99 / 0.7568	28.98 / 0.7915
CAR & EDSR (Sun and Chen 2020)	×4	52.8M	25.25 / 0.6610	25.76 / 0.6827	26.22 / 0.7037	26.69 / 0.7214	27.91 / 0.7604
IRN (Xiao et al. 2020)	×4	4.35M	25.98 / 0.6867	26.62 / 0.7096	27.24 / 0.7328	27.72 / 0.7508	28.42 / 0.7777
SAIN (Yang et al. 2023)	×4	6.49M	27.90 / 0.7745	29.05 / 0.8088	29.83 / 0.8272	30.13 / 0.8331	30.31 / 0.8367
T-SAIN (Ours)	×4	5.45M	28.08 / 0.7893	29.43 / 0.8237	30.34 / 0.8421	30.69 / 0.8483	30.92 / 0.8517

Table 2: Quantitative results (PSNR / SSIM) of image rescaling on DIV2K under distortion at different JPEG QFs.

Strategy	Param	Set14	Urban100	DIV2K
IRN	1.67M	40.79	39.92	44.32
IRN (YCbCr)	1.67M	40.47	39.33	44.02
IRN (all-zero)	1.67M	41.37	40.55	45.18
T-IRN	1.57M	41.70	41.05	45.46

Table 3: Ablation study on T-IRN: PSNR of different image rescaling strategies for ×2 image reconstruction on Set14, Urban100 and DIV2K

crease in RGB-PSNR by 0.6 to 1.1 dB across the five benchmark datasets. This improvement highlights that our training objective, which is consistent with IRN’s and employs similarity loss in the RGB domain, ensures comprehensive enhancement across the full color spectrum, avoiding any bias towards Y-channel optimization. At the ×4 scale, although some datasets do not fully surpass the metrics of the original IRN, our method consistently demonstrates superior performance across most datasets. Notably, T-IRN achieves these gains while maintaining a similar parameter count to IRN, highlighting its enhanced efficiency and effectiveness without increasing model complexity.

Ablation Study. To assess the effectiveness of T-IRN, we performed an ablation study at the ×2 scale, keeping all other parameters constant. (1) We modified IRN to process low-frequency information after converting RGB to YCbCr, without incorporating the T-InvBlock, to compare the V-InvBlock’s treatment of luminance and chrominance interactions with our approach. (2) We also tested IRN using an all-zero tensor for high-frequency information to evaluate this strategy’s impact. As shown in Table 3, simply converting to YCbCr without the T-InvBlock did not significantly enhance performance, highlighting the V-InvBlock’s limitations. In contrast, the full implementation of the T-InvBlock demonstrated clear improvements, confirming its

effectiveness. Additionally, the all-zero tensor strategy facilitated better upscaling, affirming the efficacy of both the T-InvBlock and its associated approach in T-IRN.

Qualitative Evaluation. Figure 4 shows the visual comparison of HR reconstruction results at ×2 scale between T-IRN and other methods. It is evident that T-IRN consistently recovers more intricate details in the HR images compared to other methods, including IRN.

4.3 Evaluation for T-SAIN

Quantitative Evaluation. Similarly, we evaluated T-SAIN against SAIN and several other methods previously mentioned, focusing on scenarios where the LR images undergo JPEG lossy compression with QF ranging from 30 to 90. The objective quality of the reconstructed HR images was assessed specifically on the DIV2K dataset.

As shown in Table 2, T-SAIN consistently outperforms SAIN model across various JPEG QF levels on the DIV2K dataset. At the ×2 scale, T-SAIN shows PSNR gains of 0.4 to 0.6 dB, along with improved SSIM, across different QF settings. At the ×4 scale, it continues to surpass SAIN, with PSNR improvements of 0.2 to 0.5 dB. These results highlight T-SAIN’s enhanced robustness and effectiveness in lossy compression scenarios, all while maintaining a similar parameter count to SAIN.

Ablation Study. To evaluate T-SAIN’s effectiveness, we performed ablation experiments under JPEG compression with QF values of 50, 70, and 80. (1) We applied YCbCr color space conversion to SAIN’s low-frequency branch to assess the model’s handling of luminance and chrominance information. (2) We replaced SAIN’s original GMM-based high-frequency modeling with an all-zero tensor to examine the impact of this simplification.

The results provide key insights. First, converting to YCbCr consistently improved PSNR at all QF levels, proba-

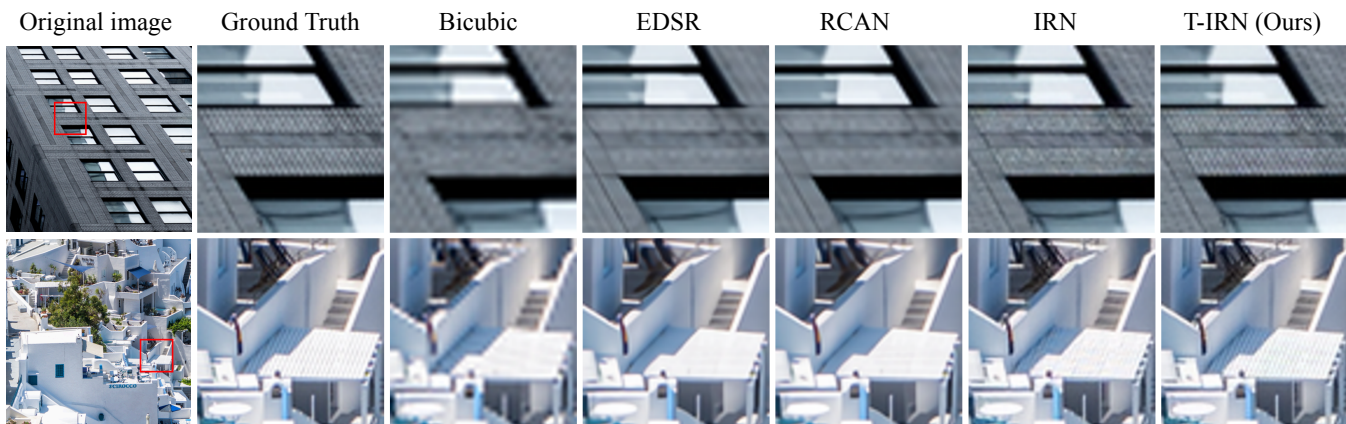


Figure 4: Qualitative Evaluation($\times 2$) for T-IRN. The shown images are 0846 and 0823 from DIV2K.

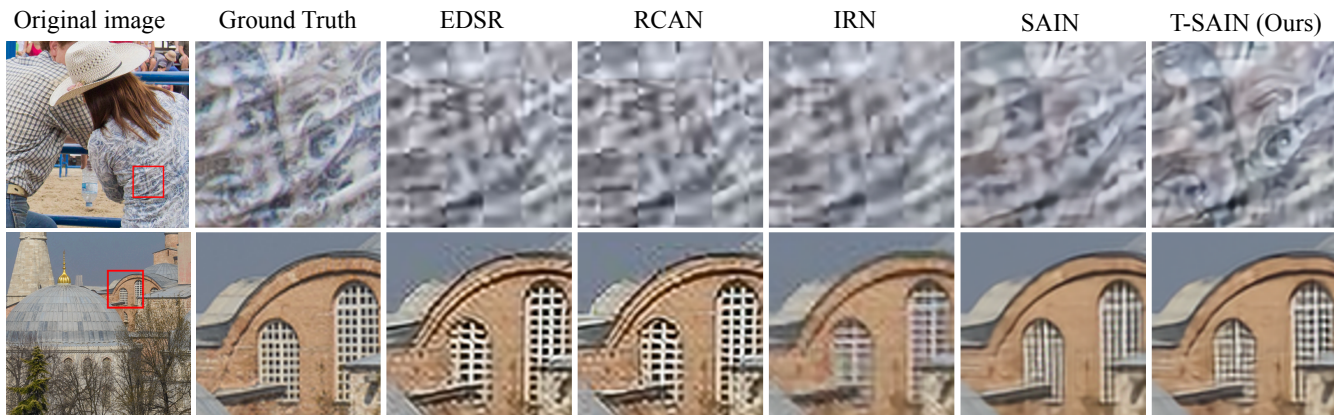


Figure 5: Qualitative Evaluation($\times 2$) for T-SAIN. The shown images are 0804 and 0890 from DIV2K. The first row shows images where the LR input was compressed with JPEG QF=30 before upscaling, while the second row shows images where the LR input was compressed with JPEG QF=90.

Strategy	Param	QF=50	QF=70	QF=80
SAIN	6.49M	29.05	29.83	30.13
SAIN (YCbCr)	6.49M	29.28	30.13	30.47
SAIN (all-zero)	6.49M	29.15	29.87	30.12
T-SAIN	5.45M	29.43	30.34	30.69

Table 4: Ablation study on T-SAIN: PSNR of different image rescaling strategies for $\times 4$ image reconstruction on DIV2K under QF=50, 70, and 80.

bly due to better alignment with JPEG’s YCbCr-based compression, which enhanced the effectiveness of the compression simulator g and improved overall reconstruction quality. Second, replacing GMM modeling with an all-zero tensor improved PSNR at QF=50 and QF=70, with only a slight decline at QF=80. This indicates that concentrating high-frequency information within the LR representation can be more effective for maintaining image quality during reconstruction. Overall, our architectural adjustments, including the tri-branch design, color space conversion, and all-zero mapping strategy, collectively enhanced performance and

robustness across compression scenarios.

Qualitative Evaluation. Figure 5 shows a qualitative comparison of T-SAIN with other methods for $\times 2$ HR reconstruction on JPEG-compressed LR images. T-SAIN clearly recovers more original details compared to other methods, notably SAIN, enhancing compression-awareness and model robustness.

5 Conclusion

In this work, we introduced the tri-branch invertible block (T-InvBlock), a novel architecture for enhancing image rescaling. By separating the low-frequency branch into luminance (Y) and chrominance (CbCr) components, T-InvBlock enables more precise processing and improves reconstruction. Our all-zero mapping strategy for high-frequency components further boosts performance. The plug-and-play design of T-InvBlock integrates seamlessly into existing models, as demonstrated in T-IRN and T-SAIN, which outperform traditional methods in both general rescaling and lossy compression scenarios. Evaluations highlight T-InvBlock’s significant advancement in image processing.

6 Acknowledgement

This work was supported in part by the National Natural Science Foundation of China under Grant U20A20184, in part by the Natural Science Foundation of Sichuan Province under Grant 2023NSFSC1972.

References

- Agustsson, E.; and Timofte, R. 2017. Ntire 2017 challenge on single image super-resolution: Dataset and study. In *Proceedings of the IEEE conference on computer vision and pattern recognition workshops*, 126–135.
- Bevilacqua, M.; Roumy, A.; Guillemot, C.; and Alberi-Morel, M. L. 2012. Low-complexity single-image super-resolution based on nonnegative neighbor embedding. In *Proceedings of the British Machine Vision Conference*, 135.1–135.10.
- Chen, H.; Hao, J.; Zhao, K.; Yuan, K.; Sun, M.; Zhou, C.; and Hu, W. 2024. CasSR: Activating Image Power for Real-World Image Super-Resolution. *arXiv preprint arXiv:2403.11451*.
- Dai, T.; Cai, J.; Zhang, Y.; Xia, S.-T.; and Zhang, L. 2019. Second-order attention network for single image super-resolution. In *Proceedings of the IEEE/CVF conference on computer vision and pattern recognition*, 11065–11074.
- Dinh, L.; Krueger, D.; and Bengio, Y. 2014. Nice: Non-linear independent components estimation. *arXiv preprint arXiv:1410.8516*.
- Dinh, L.; Sohl-Dickstein, J.; and Bengio, S. 2016. Density estimation using real nvp. *arXiv preprint arXiv:1605.08803*.
- Dong, C.; Loy, C. C.; He, K.; and Tang, X. 2015. Image super-resolution using deep convolutional networks. *IEEE transactions on pattern analysis and machine intelligence*, 38(2): 295–307.
- Guo, M.; Zhao, S.; Li, Y.; Li, J.; Zhang, L.; and Wang, Y. 2022. Invertible Single Image Rescaling via Steganography. In *2022 IEEE International Conference on Multimedia and Expo (ICME)*, 1–6. IEEE.
- Huang, J.-B.; Singh, A.; and Ahuja, N. 2015. Single image super-resolution from transformed self-exemplars. In *Proceedings of the IEEE conference on computer vision and pattern recognition*, 5197–5206.
- Jain, A. K. 1989. *Fundamentals of digital image processing*. Prentice-Hall, Inc.
- Kim, H.; Choi, M.; Lim, B.; and Lee, K. M. 2018. Task-aware image downscaling. In *Proceedings of the European Conference on Computer Vision (ECCV)*, 399–414.
- Kingma, D. P.; and Ba, J. 2014. Adam: A method for stochastic optimization. *arXiv preprint arXiv:1412.6980*.
- Kobyzev, I.; Prince, S. J.; and Brubaker, M. A. 2020. Normalizing flows: An introduction and review of current methods. *IEEE transactions on pattern analysis and machine intelligence*, 43(11): 3964–3979.
- Li, Y.; Liu, D.; Li, H.; Li, L.; Li, Z.; and Wu, F. 2018. Learning a convolutional neural network for image compact-resolution. *IEEE Transactions on Image Processing*, 28(3): 1092–1107.
- Liang, J.; Lugmayr, A.; Zhang, K.; Danelljan, M.; Van Gool, L.; and Timofte, R. 2021. Hierarchical conditional flow: A unified framework for image super-resolution and image rescaling. In *Proceedings of the IEEE/CVF International Conference on Computer Vision*, 4076–4085.
- Lienhart, R.; and Maydt, J. 2002. An extended set of haar-like features for rapid object detection. In *Proceedings. international conference on image processing*, volume 1, I–I. IEEE.
- Lim, B.; Son, S.; Kim, H.; Nah, S.; and Mu Lee, K. 2017. Enhanced deep residual networks for single image super-resolution. In *Proceedings of the IEEE conference on computer vision and pattern recognition workshops*, 136–144.
- Liu, Y.; Qin, Z.; Anwar, S.; Ji, P.; Kim, D.; Caldwell, S.; and Gedeon, T. 2021. Invertible denoising network: A light solution for real noise removal. In *Proceedings of the IEEE/CVF conference on computer vision and pattern recognition*, 13365–13374.
- Lu, Y.; Li, X.; Pei, Y.; Yuan, K.; Xie, Q.; Qu, Y.; Sun, M.; Zhou, C.; and Chen, Z. 2024. Kvq: Kwai video quality assessment for short-form videos. In *Proceedings of the IEEE/CVF Conference on Computer Vision and Pattern Recognition*, 25963–25973.
- Martin, D.; Fowlkes, C.; Tal, D.; and Malik, J. 2001. A database of human segmented natural images and its application to evaluating segmentation algorithms and measuring ecological statistics. In *Proceedings Eighth IEEE International Conference on Computer Vision. ICCV 2001*, volume 2, 416–423. IEEE.
- Mo, Q.; Ding, Y.; Hao, J.; Zhu, Q.; Sun, M.; Zhou, C.; Chen, F.; and Zhu, S. 2025. OAPT: Offset-Aware Partition Transformer for Double JPEG Artifacts Removal. In *European Conference on Computer Vision*, 38–56. Springer.
- Pan, Z.; Li, B.; He, D.; Wu, W.; and Ding, E. 2023. Effective invertible arbitrary image rescaling. In *Proceedings of the IEEE/CVF Winter Conference on Applications of Computer Vision*, 5416–5425.
- Pan, Z.; Li, B.; He, D.; Yao, M.; Wu, W.; Lin, T.; Li, X.; and Ding, E. 2022. Towards bidirectional arbitrary image rescaling: Joint optimization and cycle idempotence. In *Proceedings of the IEEE/CVF Conference on Computer Vision and Pattern Recognition*, 17389–17398.
- Poynton, C. 2012. *Digital video and HD: Algorithms and Interfaces*. Elsevier.
- Qin, R.; Sun, M.; Zhou, C.; and Wang, B. 2025. A New Dataset and Framework for Real-World Blurred Images Super-Resolution. In *European Conference on Computer Vision*, 56–75. Springer.
- Qu, Y.; Yuan, K.; Zhao, K.; Xie, Q.; Hao, J.; Sun, M.; and Zhou, C. 2025. Xpsr: Cross-modal priors for diffusion-based image super-resolution. In *European Conference on Computer Vision*, 285–303. Springer.
- Quan, Y.; Tan, X.; Huang, Y.; Xu, Y.; and Ji, H. 2024. Enhancing Underwater Images via Asymmetric Multi-Scale Invertible Networks. In *Proceedings of the 32nd ACM International Conference on Multimedia*, 6182–6191.

- Rezende, D.; and Mohamed, S. 2015. Variational inference with normalizing flows. In *International conference on machine learning*, 1530–1538. PMLR.
- Son, H.; Kim, T.; Lee, H.; and Lee, S. 2021. Enhanced standard compatible image compression framework based on auxiliary codec networks. *IEEE Transactions on Image Processing*, 31: 664–677.
- Sun, W.; and Chen, Z. 2020. Learned image downscaling for upscaling using content adaptive resampler. *IEEE Transactions on Image Processing*, 29: 4027–4040.
- Wallace, G. K. 1991. The JPEG still picture compression standard. *Communications of the ACM*, 34(4): 30–44.
- Wang, X.; Yu, K.; Wu, S.; Gu, J.; Liu, Y.; Dong, C.; Qiao, Y.; and Change Loy, C. 2018. Esrgan: Enhanced super-resolution generative adversarial networks. In *Proceedings of the European conference on computer vision (ECCV) workshops*, 0–0.
- Wang, Z.; Bovik, A. C.; Sheikh, H. R.; and Simoncelli, E. P. 2004. Image quality assessment: from error visibility to structural similarity. *IEEE transactions on image processing*, 13(4): 600–612.
- Xiao, M.; Zheng, S.; Liu, C.; Lin, Z.; and Liu, T.-Y. 2023. Invertible rescaling network and its extensions. *International Journal of Computer Vision*, 131(1): 134–159.
- Xiao, M.; Zheng, S.; Liu, C.; Wang, Y.; He, D.; Ke, G.; Bian, J.; Lin, Z.; and Liu, T.-Y. 2020. Invertible image rescaling. In *European Conference on Computer Vision*, 126–144. Springer.
- Xie, Q.; Yuan, K.; Qu, Y.; Wu, M.; Sun, M.; Zhou, C.; and Zhu, J. 2024. QPT-V2: Masked Image Modeling Advances Visual Scoring. In *Proceedings of the 32nd ACM International Conference on Multimedia*, 2709–2718.
- Xing, J.; Hu, W.; Xia, M.; and Wong, T.-T. 2023. Scale-arbitrary invertible image downscaling. *IEEE Transactions on Image Processing*.
- Yang, J.; Guo, M.; Zhao, S.; Li, J.; and Zhang, L. 2023. Self-asymmetric invertible network for compression-aware image rescaling. In *Proceedings of the AAAI Conference on Artificial Intelligence*, volume 37, 3155–3163.
- Yuan, K.; Liu, H.; Li, M.; Sun, M.; Sun, M.; Gong, J.; Hao, J.; Zhou, C.; and Tang, Y. 2024. PTM-VQA: Efficient Video Quality Assessment Leveraging Diverse PreTrained Models from the Wild. In *Proceedings of the IEEE/CVF Conference on Computer Vision and Pattern Recognition*, 2835–2845.
- Zeyde, R.; Elad, M.; and Protter, M. 2010. On single image scale-up using sparse-representations. In *International conference on curves and surfaces*, 711–730. Springer.
- Zhang, Y.; Li, K.; Li, K.; Wang, L.; Zhong, B.; and Fu, Y. 2018a. Image super-resolution using very deep residual channel attention networks. In *Proceedings of the European conference on computer vision (ECCV)*, 286–301.
- Zhang, Y.; Tian, Y.; Kong, Y.; Zhong, B.; and Fu, Y. 2018b. Residual dense network for image super-resolution. In *Proceedings of the IEEE conference on computer vision and pattern recognition*, 2472–2481.
- Zhu, Q.; Hao, J.; Ding, Y.; Liu, Y.; Mo, Q.; Sun, M.; Zhou, C.; and Zhu, S. 2024. CPGA: Coding Priors-Guided Aggregation Network for Compressed Video Quality Enhancement. In *Proceedings of the IEEE/CVF Conference on Computer Vision and Pattern Recognition*, 2964–2974.